Corrosion Science 140 (2018) 1–7

Contents lists available at ScienceDirect

Corrosion Science

journal homepage: www.elsevier.com/locate/corsci

# Quasi-in-situ observing the growth of native oxide film on the $FeCr_{15}Ni_{15}$ austenitic alloy by TEM

B. Zhang[a,*,1], X.Y. San[a,1], X.X. Wei[a], B. Wu[a], S.J. Zheng[a], Y.T. Zhou[a], X.H. Shao[a], Q.Q. Jin[a], L.X. Yang[a], E.E. Oguzie[b], X.L. Ma[a,c,**]

[a] Shenyang National Laboratory for Materials Science (SYNL), Institute of Metal Research, Chinese Academy of Sciences, Wenhua Road 72, 110016, Shenyang, China
[b] Electrochemistry and Materials Science Research Laboratory, Department of Chemistry, Federal University of Technology Owerri, PMB 1526, Owerri, Nigeria
[c] State Key Lab of Advanced Processing and Recycling on Non-ferrous Metals, Lanzhou University of Technology, Lanzhou, 730050, China

ARTICLE INFO

*Keywords:*
$FeCr_{15}Ni_{15}$ single crystal
TEM
Oxide film

ABSTRACT

Element Cr imparts non-crystallinity effect on the oxide film on iron. Therefore, in contrast with the oxidation of iron, the oxidation process of Fe-Cr alloys is more complicated. By means of high angle annular dark field scanning transmission electron microscopic (HAADF-STEM) imaging combined with electron-energy loss spectroscopy (EELS) and super-X electron dispersed spectroscopy (Super-X EDS) techniques in an aberration-corrected TEM, we have clarified the evolution in the oxide film formed on an $FeCr_{15}Ni_{15}$ alloy. The oxide film is identified to be amorphous at the initial oxidation stage, but tends to become crystalline in the inner layer after aging in air.

## 1. Introduction

The nanometer-thick passive films on metals remarkably retard the corrosion rate and render the metals highly resistant to general corrosion. In a broad sense, passive films include the air-formed oxide film (e.g. native oxide film) in addition to the anodically polarized passive film in an electrolyte. The structure and composition as well as the growth of the passive film have been long-standing issues attracting a lot of attention from the scientific community. In dealing with these issues, the interaction of oxygen with iron surfaces has been well studied, both experimentally [1–14] and theoretically [15,16], since the phenomenon of passivity was first reported for iron. This is most often accomplished by using single-crystal Fe [1–6,8–12] or nanoparticles [13,14,17–20]. A common consensus so far is that the oxide layer formed during initial oxidation comprises primarily of spinel $\gamma$-$Fe_2O_3$ /$Fe_3O_4$. It has also been reported that FeO is formed initially, with subsequent heating leading to the transformation of FeO to $\gamma$-$Fe_2O_3$/ $Fe_3O_4$. Although the oxide film on iron is usually crystalline, incorporation of Cr as an alloying element has been found to impart non-crystallinity on the oxide film [21–24]. As a result, the Cr-rich passive film on Fe-Cr alloys and stainless steels is usually considered to be almost amorphous [21–26].

Recently, core-shell structured iron nanoparticles originating from the oxidation process have drawn great attention due to their potential for applications in many fields [14,20,27–30]. The typical Fe core-oxide shell structure implies that there is significant outward diffusion of Fe and a minor inward diffusion of oxygen during the oxidation of iron [14]. The oxidation process of Fe-Cr alloy is however more complicated than that of iron. The tendency of Cr to render the passive film non-crystalline might result from alteration of the oxide growth process, which could be clarified by monitoring the evolution of the oxide film at various stages, ranging from the initial formation to subsequent growth and upon long-term aging in air.

Various ex-situ techniques have been employed in investigating passive films. These include X-ray photoelectron spectroscopy (XPS) [24,31–36], ion-scattering spectroscopy (ISS) [37], auger electron spectroscopy (AES) [31,32,38], secondary-ion mass spectroscopy (SIMS) [31,32,39,40] etc. Again, in-situ techniques such as scanning tunneling microscopy (STM) [21,24–26,41] and X-ray absorption near edge structure (XANES) [42–44] have also been applied. However, no technique has so far succeeded in simultaneously providing both chemical and structural information on the evolution of passive films. Interestingly, aberration-corrected transmission electron microscopy (Cs-corrected TEM) has tremendous potential for atomic-scale resolution of

* Corresponding author.
** Corresponding author at: Shenyang National Laboratory for Materials Science (SYNL), Institute of Metal Research, Chinese Academy of Sciences, Wenhua Road 72, 110016, Shenyang, China.
*E-mail addresses:* bozhang@imr.ac.cn (B. Zhang), xlma@imr.ac.cn (X.L. Ma).
[1] These authors contributed equally to this work.

https://doi.org/10.1016/j.corsci.2018.06.029
Received 15 March 2018; Received in revised form 4 June 2018; Accepted 18 June 2018
Available online 22 June 2018
0010-938X/ © 2018 Elsevier Ltd. All rights reserved.

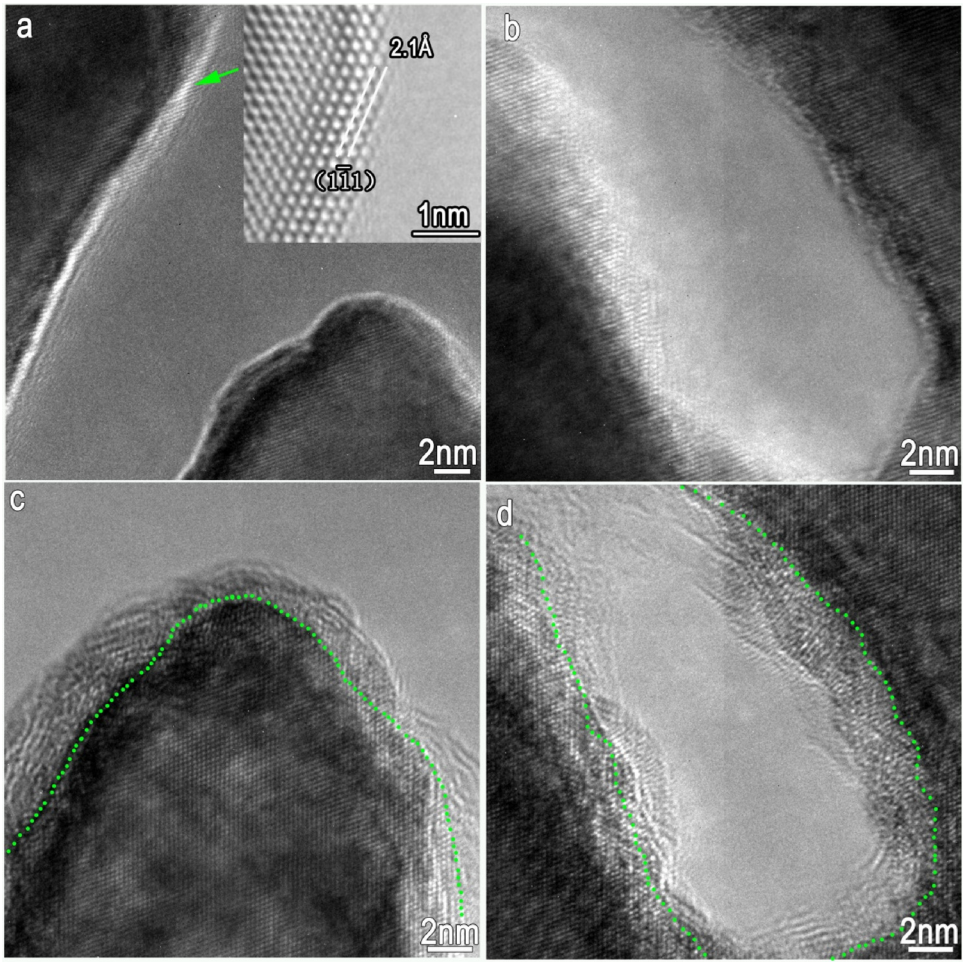


**Fig. 1.** Bright-field TEM image showing the oxide film growth on freshly prepared side planes. (a–b) TEM images showing two different-shaped holes formed by the convergent-beam irradiation. (c–d) TEM images taken in the same regions in (a) and (b), respectively, after aging in the air for 3 days. A thin-layer of an amorphous oxide film is clearly seen. The inset in (a) is the aberration-corrected HRTEM images (corresponding to the region marked by the green arrow in a) showing the sharp edge of the fresh side plane formed by the convergent beam irradiation. (For interpretation of the references to colour in this figure legend, the reader is referred to the web version of this article).

the nature of passive films across the entire film, ranging from the surface to the metal/film interface. Some researchers have also attempted to use the TEM technique for ex-situ characterization of passive films [45–49]. However, accurate monitoring of the evolution of oxide films at various oxidation stages, especially as regards acquisition of the initial chemical and structural information at the early-stages of oxidation, requires in-situ TEM observation.

In order to effectively study the oxidation process, it is essential that the original oxide-free surface must be available. In the present work, we used electron-beam cutting method to obtain the fresh oxide-free side planes. We then performed high resolution HAADF-STEM imaging, EELS analysis, as well as super-X EDS measurements in an aberration-corrected TEM in order to examine, in a quasi-in-situ manner and at an atomic scale, the oxidation process of a model single crystalline $FeCr_{15}Ni_{15}$ austenitic alloy. This study provides some virtual experimental insights on the oxidation of Fe-Cr alloy by acquiring information at the early-oxidation stage as well as during successive evolution.

## 2. Experimental

### 2.1. Single crystal alloy preparation and orientation determination

$FeCr_{15}Ni_{15}$ (wt.%) single crystal alloy was used as matrix for the growth of native oxide film. The single crystal can be treated as an austenite single phase alloy with trace amounts of other phases.

The orientation was determined by single-crystal X-ray diffractometery. Two low-index crystallographic orientations [001] and [110] were obtained.

### 2.2. TEM specimen preparation

The alloy specimen was sliced into pieces with the thickness of 300 μm, with surface being parallel to (110) crystallographic plane. The piece was ground to 80 μm using silicon carbide papers and then die-cut into disks with diameter of 3 mm. During grinding of the piece specimens with varied grit silicon carbide papers, we tried our best to keep the surface level in order to avoid artificial deviations from the crystallographic plane. The disk samples were ground using variant grit silicon carbide papers, up to 20 μm, polished with diamond paste, and finally thinned by ion-milling to achieve electron transparency.

### 2.3. Quasi-in-situ observation of the growth of native oxide film

In order to obtain the fresh oxide-free side planes, we applied an electron-beam cutting method in TEM. We first irradiated the thin zone of the TEM specimen by focusing the electron beam on the specimen to yields a through hole, with the exposure of fresh side planes. The width of the hole was a few nanometers and the depth about 100 nm (e.g. the thickness of the thin zone of the TEM specimen). The residual atmosphere in the TEM column was $10^{-8}$ Torr grade, which is favorable for the initial formation of native oxide film and thus enabled us to observe the initial growth of the oxide film on the fresh side planes. After recording the initial growth in the first round of observations, the specimen was exposed in air for varied time intervals and then transferred into the TEM for further investigation, with special attention on the evolution of the oxide film. This enabled a quasi-continuous approach for monitoring the evolution of the native oxide film.

### 2.4. TEM techniques

An aberration-corrected TEM (Titan$^{3TM}$ G2 60–300 microscope fitted with a high brightness field emission source, a monochromator, and double Cs correctors from CEOS) was operated at 300 kV for high resolution TEM (HRTEM) and high resolution HAADF scanning transmission electron microscopic (HR-HAADF-STEM) imaging. Electron energy loss spectroscopy (EELS) measurements were conducted in STEM mode. The convergence angle of the electron beam was approximately 25 m rad, with 1 nm probe beam diameter.

## 3. Results

Fig. 1 is the bright-field TEM image showing the growth of oxide film on the fresh side planes. The fresh side planes (Fig. 1a and b) were formed by the convergent beam irradiation, with distinct and sharp edges (Fig. 1 inset). On aging in the TEM column for a few hours, the fresh planes were seen to form a thin-layer (1 ~ 1.5 nm) amorphous film (typically 3 h for distinct amorphous film). The thickness of the amorphous film reached about 2–5 nm after 3 days of exposure to air (as shown in Fig. 1c and d) and about 8 nm after 3 month, filling up the hole (Fig. 2). Interestingly, the hitherto amorphous film immediately adjacent to the matrix became crystalline, even though the outer layer is still remained amorphous.

The HAADF-STEM imaging mode facilitates clear visualization of crystalline lattices, since this mode is insensitive to any possible amorphous constituent leftover from incomplete crystallization. Fig. 3 shows the high-resolution HAADF-STEM images (along [110] direction) of the same area in the film after aging in air for 3 months (Fig. 3a) and 6 months (Fig. 3b), respectively. The amorphous zone is extremely thin and thus shows very dark contrast. The amorphous zone after aging in air for 6 months did not become more crystalline, while the crystalline belt as well showed no evidence of further evolution, indicating that the film has achieved an equilibrium state. Evidently, the film has a bi-layer equilibrium structure with an inner crystalline layer and an outer amorphous layer. The inner crystalline layer includes two types of structures which were identified to be spinel (colored in green) and NaCl structures (colored in red) (Fig. 3a inset). The NaCl-structured cluster, with a lattice parameter of 0.43 nm, often appeared adjacent to the matrix, whereas the spinel zone seemed removed from the matrix, isolated by the NaCl-structured cluster as shown in Fig. 3. Two regions marked with the red and green circles in Fig. 3b, corresponding to the NaCl and spinel structure respectively, were chosen to perform EELS analysis and the spectra (enlarged view) covering the Fe-$L_{2,3}$ edges are shown in Fig. 3c. Compared with the NaCl-structured region, the Fe-$L_2$ and $L_3$ edges corresponding to the spinel region can be seen to shift towards the higher energy loss, which implies an increase in the average oxidation state of transition metal cations. The lower oxidation state of iron should be bivalent iron and thus the NaCl structured cluster is identified to contain FeO (the lattice parameter 0.43 nm of FeO is coincident with that of the NaCl structured cluster). The increased average oxidation state of iron indicates that the spinel cluster contains bivalent as well as trivalent iron and is in tandem with the $Fe_3O_4$.

Although the EELS is successful in determining the valence state of transition metals like Ti, Mn and Co, it fails to treat the valence state of Cr. Actually, some studies have attempted to analyze the Cr valence using the white line ratio of $L_3/L_2$, as well as the Cr-$L_{2,3}$ edge and the coordinated O-K edge onset extracted from the full EELS spectra. The resultant data is however often highly scattered. By means of super-X EDS mapping experiments, we successfully obtained the element distribution in the film, as shown in Fig. 4. From the element O map, we identified the film to be an oxide film, namely air-formed passive film. Combining the Fe and Cr maps, a well-defined bi-layer passive film can be seen, where the inner layer, adjacent to the metal, is enriched in Cr and depleted in Fe, while the outer layer is depleted in Cr and enriched in Fe. It is noteworthy that the outer layer is not absolutely homogeneous in composition, wherein the amorphous zone (darkest contrast shown in the HAADF-STEM image of Fig. 4) is slightly enriched in Cr and depleted in Fe. Combining the super-X EDS data with the high-resolution HAADF-STEM image, it becomes very clear that the inner NaCl-structured crystalline layer is enriched in Cr and depleted in Fe, the middle spinel layer is enriched in Fe and depleted in Cr, and the outer amorphous layer is slightly enriched in Cr. On the matrix side, immediately adjacent to the oxide film/matrix interface, there exists a layer with Ni enrichment, which is similar to that in the passive film anodically formed in an electrolyte [25,47,49,50]. From the combined map in Fig. 4, the feature of Ni-rich/Cr-rich/Fe-rich/slightly-Cr-rich structure in the oxide film as well as near the interface is well-distinguished. Formation of fcc $Cr_2O_3$ oxide film on pure Cr nano-particles, with a lattice parameter of 0.407 nm has been reported [51]. Based on the aforementioned, the inner Cr-rich NaCl-structured cluster should be a mixed oxide containing $Cr_2O_3$·FeO, and the middle Fe-rich spinel cluster should be $Fe_3O_4$·$CrFe_2O_4$ (Cr partially substitutes $Fe^{3+}$ positions).

The elemental composition in the initially-formed amorphous oxide film was also analyzed using super-X EDS mapping technique. As shown in Fig. 5, a well-defined layer of amorphous oxide formed after exposure in air for 3 h (Fig. 5a). Super-X EDS mapping analysis, performed in HAADF mode (corresponding to Fig. 5d), also shows a bi-layer structure with Cr-rich inner layer and Fe-rich outer layer.

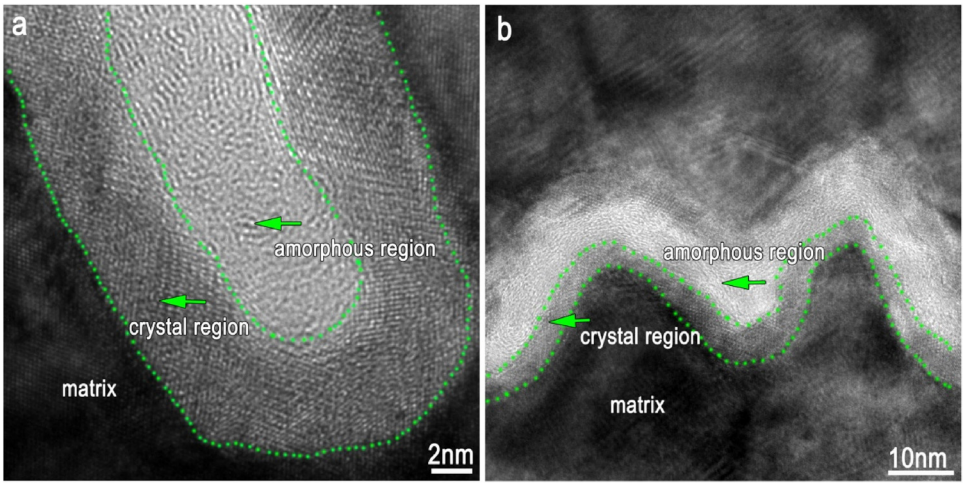


**Fig. 2.** HRTEM images showing the thickening of the film and the inception of partial crystallinity of the amorphous film after aging in ambient air for 3 months. (a) HRTEM image showing that the film has filled up the hole formed by beam irradiation. The hitherto amorphous film immediately adjacent to the matrix has become crystalline. (b) HRTEM image showing a large area of the amorphous film and a belt immediately adjacent to the matrix, which has become crystalline. The crystalline belt has uneven width and relatively thicker at the zone with larger curvature and thinner at smaller curvature.

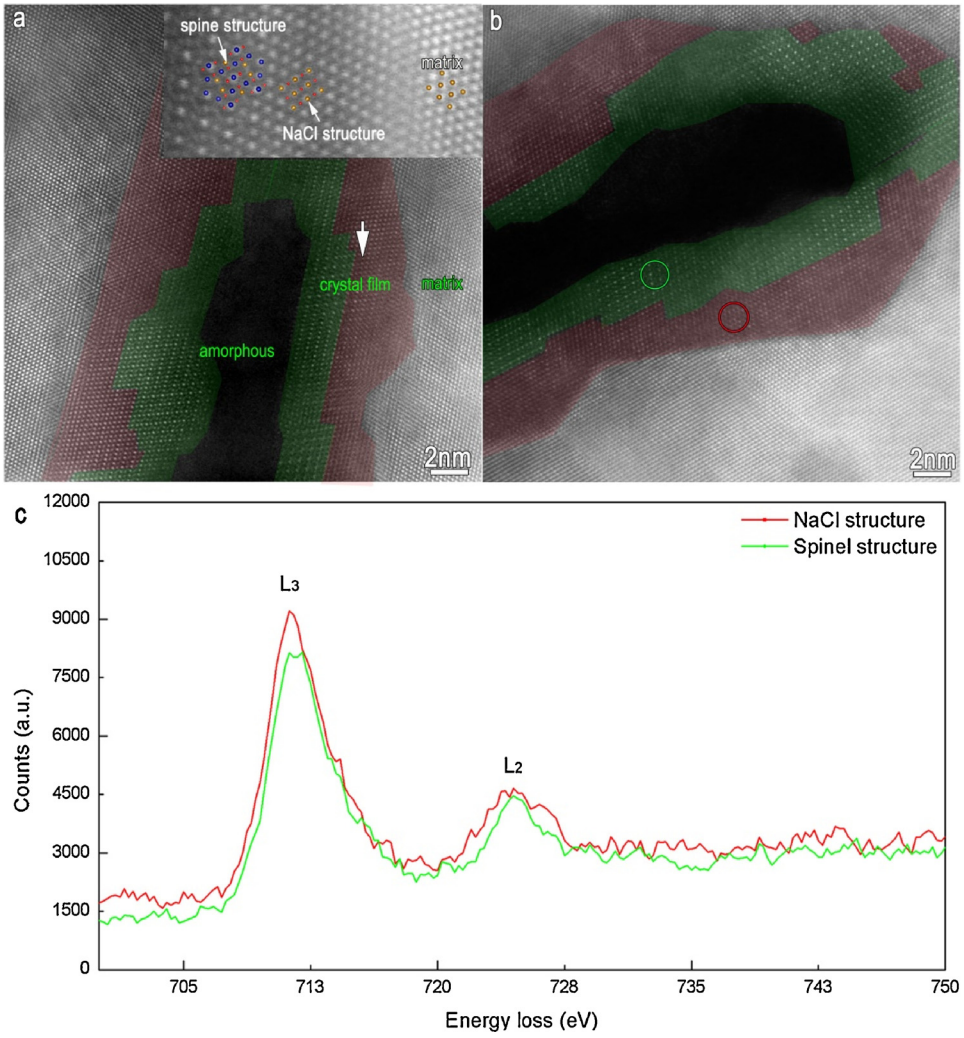


**Fig. 3.** Aberration-corrected high-resolution HAADF-STEM images of the same region in the film after aging in air for 3 months (a) and 6 months (b). The inset in (a) is the zoom-in image of the region marked by the white arrow in (a). The two different lattice structrues are identified as spinel and NaCl structures (along [110] direction), respectively. (c) EELS analysis, performed on the NaCl-structured (marked by the red circle) and spinel zone (marked by the green circle), showing the EELS edges of Fe-$L_{2,3}$. A slight chemical shift to higher energy loss for the spinel zone is observed. (For interpretation of the references to colour in this figure legend, the reader is referred to the web version of this article).

## 4. Discussion

Effective identification of the structure and chemistry of oxide films during different stages of oxidation makes it possible to reconstruct the oxidation process, as illustrated in Fig. 6. At the initial oxidation stage, a thin layer of amorphous Cr-rich oxide forms on the pristine surface (Fig. 6a and b). At the latter stages, the oxidation process typically involves the diffusion of metal ions outwards and/or oxygen inwards. It has been observed during the oxidation of iron, that the outward diffusion of Fe is the dominant mass transport process [8,14,52–57], but the oxygen inwards diffusion is also expected [14]. This assertion is supported by the fact that the diameter of the voids formed in the center of the Fe nanoparticle is much smaller than the initial Fe particle size, implying that the oxide/Fe interface moves to the matrix side. Comparatively, we monitored the evolution of the oxide film on the $FeCr_{15}Ni_{15}$ alloy and observed that the oxide/$FeCr_{15}Ni_{15}$ matrix interface did not move to the matrix side, totally different from what is observed with iron. This implies that the inward diffusion of oxygen is probably retarded remarkably by the initially formed Cr-rich oxide layer, and the oxidation reaction front is at the oxide/oxygen interface rather than the $FeCr_{15}Ni_{15}$/oxide interface. The dominant outward diffusion of Fe yields a bi-layer structure with an inner Cr-rich layer and an outer Fe-rich layer (Fig. 6c). On long-term aging in air, the initially-formed amorphous oxide becomes a crystalline NaCl-structured $Cr_2O_3$·FeO mixture (Fig. 6d). During the aging period, the NaCl-structure would inevitably be partially transformed into a spinel structure via further oxidation, wherein Fe (II) is oxidized to a higher valance Fe (III). This further oxidation would occur inwards, yielding the spinel structure at the outer layer (Fig. 6e). Meanwhile, $Cr_2O_3$ might be partially oxidized to the higher valence state of $CrO_3$, constituting the outermost amorphous oxide layer (Fig. 6e). The standard free enthalpies of $CrO_3$ and $Cr_2O_3$ are $-141$ and $-136$ kcal mol$^{-1}$, respectively. Because these values are so close, these phases are likely to coexist. The combination of the two vastly different oxidation states of Cr would provide a condition for significant bond flexibility that may lead to a relatively stable non-crystalline oxide [58].

It is well known that passive films on bulk metals are very thin, usually 2–3 nm. In contrast, the oxide film formed on the wall of the thin-foil specimen used in the present work was thicker, with equilibrium thickness estimated to be about 8 nm. The equilibrium thickness actually is highly dependent on the diffusion of the reactive species in the oxide film [22], such as metal (Fe and/or Cr) ions outwards and/or O atoms inwards diffusion. In an earlier combined electrochemical and surface analytical study, it was shown that $Fe^{3+}$ layers may act as a barrier for ion transport, and therefore may cause oxidation rates to diminish (oxide growth virtually stops) [59]. For the bulk metal, the bulk diffusion rate of the metal ions is very low at room temperature, yielding a very thin oxide film (2–3 nm). By contrast, for the thin-foil specimen with thickness of only ~100 nm scale, the surface diffusion would be remarkably enhanced, resulting in a thicker oxide film. It is worthwhile to note that the enhanced-surface-diffusion dominated growth would lead to a wedge-shaped oxide film, in which the oxide grows thinner from the inner to the outer layer, as illustrated in Fig. 7. Indeed, we did observe such a wedge-shaped oxide film, as revealed by

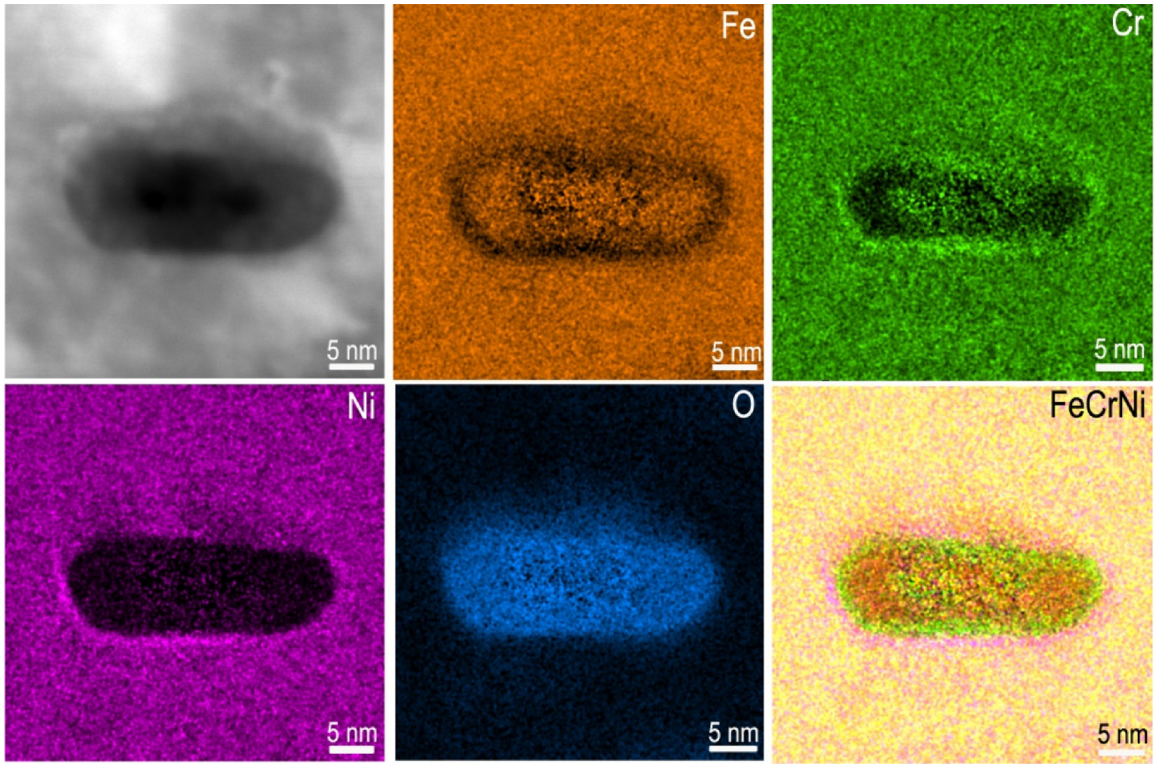


**Fig. 4.** Super-X EDS mapping showing the element distribution within the film and near the interfaces.

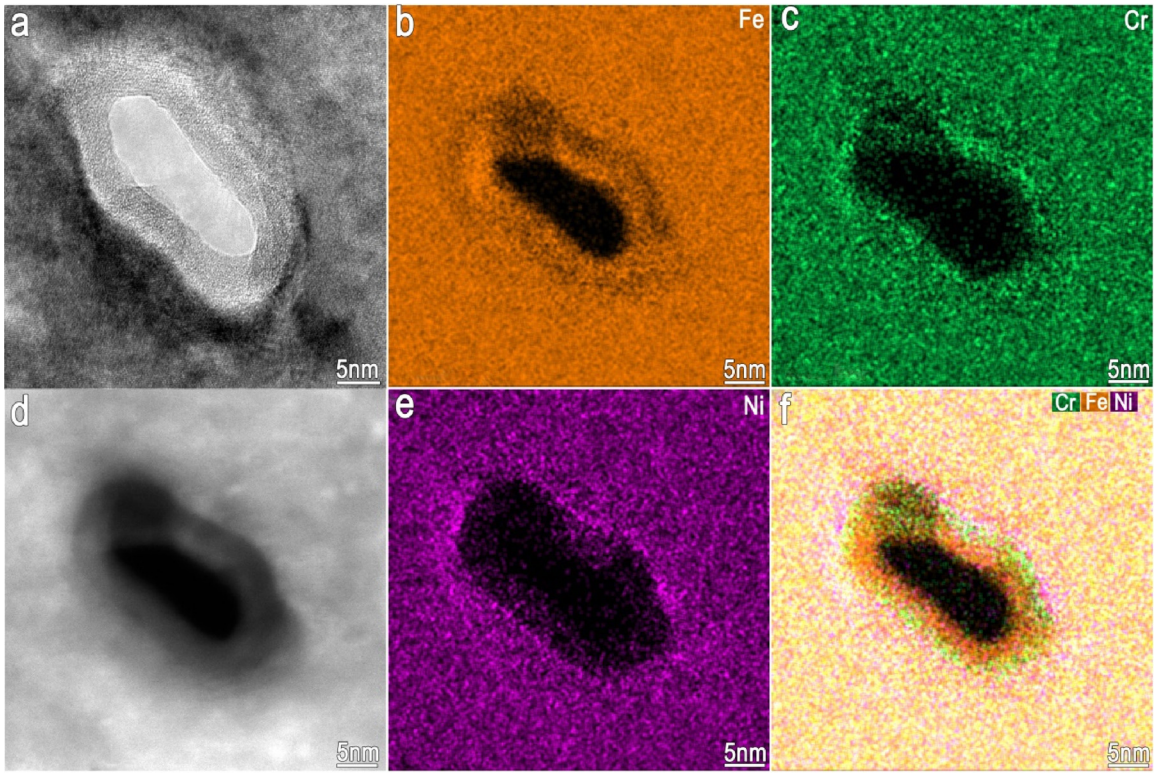


**Fig. 5.** Super-X EDS mapping showing the element distribution within the initially-formed amorphous oxide film and near the interfaces. (a) Bright-field TEM image showing a thin layer of amorphous oxide film formed on the fresh side planes after exposure for 3 h in air. (b, c) Elemental maps of Fe and Cr, respectively, in the amorphous oxide film. (d) HAADF-STEM image corresponding to (a). (e, f) Elemental maps of Ni and Cr/Fe/Ni, respectively, in the amorphous oxide film.

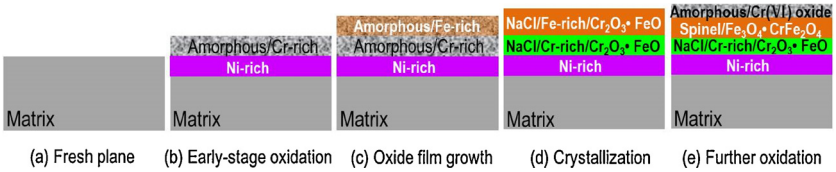


**Fig. 6.** Schematic maps illustrating the oxidation process of $FeCr_{15}Ni_{15}$ alloy in air.


**Fig. 7.** Schematic map illustrating that enhanced surface diffusion yields a thicker wedge-shaped oxide film on the wall of the thin foil matrix.

the evident contrast difference, with a brighter inner layer and darker outer layer in the HAADF mode. Even at the center of the hole, the amorphous region appears almost black in contrast, indicating a very thin film. It is noteworthy that the HAADF mode image provides an incoherent image using high angle scattered electrons, where the contrast is strongly dependent on the scattering ability of heavy atoms and sensitive to the thickness. Therefore, the thinner the oxide film is, the darker the contrast will be.

## 5. Conclusion

Fresh oxide-free side planes were obtained on $FeCr_{15}Ni_{15}$ single crystal alloy using the electron-beam cutting method. By means of HAADF-STEM imaging combined with EELS and EDS analysis, we have identified the structure and chemistry of the oxide film at various oxidation stages and reconstructed the oxidation process. The amorphous film formed at the initial oxidation stage gradually thickened and following long-term aging in air, became crystalline around the region immediately adjacent to the matrix. Further oxidation of Fe (II) to Fe (III) led to a partial transformation from NaCl-type to spinel-type structure, while the outmost amorphous oxide layer could be attributed to oxidation of Cr (III) to Cr (VI). The enhanced-surface-diffusion dominant growth of the oxide resulted in a thicker wedge-shaped oxide film.

## Data availability

The raw/processed data required to reproduce these findings cannot be shared at this time due to legal or ethical reasons.

## Acknowledgements

This work is supported by the National Natural Science Foundation of China (No. 51771212, 11327901, 51390473), the Key Research Program of Frontier Sciences CAS (QYZDJ-SSW-JSC010), the Innovation Fund in IMR (2017-ZD05). The authors are grateful to Prof. H. Wei for the help with the single crystal growth, Dr. J. Wang at Thermo Fisher Scientific Shanghai Nanoport for Super-X EDS mapping.

## References

[1] C. Leygraf, S. Ekelund, Leed-aes study of oxidation of Fe (110) and Fe (100), Surf. Sci. 40 (1973) 609–635.
[2] K. Ueda, R. Shimizu, Initial oxidation studies on Fe (100) by means of photoelectric work function measurements combined with Auger-electron spectroscopy, Surf. Sci. 43 (1974) 77–87.
[3] G.W. Simmons, D.J. Dwyer, Leed-aes study of initial-stages of oxidation of Fe (001), Surf. Sci. 48 (1975) 373–392.
[4] C.F. Brucker, T.N. Rhodin, Oxygen-chemisorption and reaction on alpha-Fe (100) using photoemission and low-energy electron-diffraction, Surf. Sci. 57 (1976) 523–539.
[5] C.R. Brundle, T.J. Chuang, K. Wandelt, Core and valence level photoemission studies of iron-oxide surfaces and oxidation of iron, Surf. Sci. 68 (1977) 459–468.
[6] T. Guo, M.L. Denboer, Extended appearance-potential fine-structure measurements of clean and oxidized iron surfaces, Phys. Rev. B 38 (1988) 3711–3717.
[7] M. Arbab, J.B. Hudson, The kinetics and mechanism of oxygen-uptake on a polycrystalline iron surface, Surf. Sci. 206 (1988) 317–337.
[8] G.W.R. Leibbrandt, G. Hoogers, F. Habraken, Thin oxide film growth on Fe (100), Phys. Rev. Lett. 68 (1992) 1947–1950.
[9] M.W. Ruckman, J. Chen, M. Strongin, E. Horache, Oxidation of iron films at 25 k and the reactive oxidation of iron in solid oxygen, Phys. Rev. B 45 (1992) 14273–14278.
[10] S.J. Roosendaal, I. Giebels, A.M. Vredenberg, F. Habraken, Determination of photoelectron attenuation lengths in thin oxide films on iron surfaces using quantitative XPS and elastic recoil detection, Surf. Interface Anal. 26 (1998) 758–765.
[11] S.J. Roosendaal, B. van Asselen, J.W. Elsenaar, A.M. Vredenberg, F. Habraken, The oxidation state of Fe (100) after initial oxidation in $O_2$, Surf. Sci. 442 (1999) 329–337.
[12] S.J. Roosendaal, A.M. Vredenberg, F. Habraken, Oxidation of iron: the relation between oxidation kinetics and oxide electronic structure, Phys. Rev. Lett. 84 (2000) 3366–3369.
[13] K.K. Fung, B.X. Qin, X.X. Zhang, Passivation of alpha-Fe nanoparticle by epitaxial gamma-$Fe_2O_3$ shell, Mater. Sci. Eng. A 286 (2000) 135–138.
[14] C.M. Wang, D.R. Baer, L.E. Thomas, J.E. Amonette, J. Antony, Y. Qiang, G. Duscher, Void formation during early stages of passivation: initial oxidation of iron nanoparticles at room temperature, J. Appl. Phys. 98 (2005) 094308.
[15] G. Grenet, Y. Jugnet, T.M. Duc, M. Kibler, FeO valence band photoemission spectra, J. Chem. Phys. 72 (1980) 218–220.
[16] G. Grenet, Y. Jugnet, T.M. Duc, M. Kibler, On the interpretation of $3d^N$ ions photoemission spectra .1. A comparative-study for the valence band of FeO, CoO, and NiO, J. Chem. Phys. 74 (1981) 2163–2173.
[17] K. Haneda, A.H. Morrish, Oxidation of aerosoled ultrafine iron particles, Nature 282 (1979) 186–188.
[18] T.C. Rojas, J.C. Sanchez-Lopez, J.M. Greneche, A. Conde, A. Fernandez, Characterization of oxygen passivated iron nanoparticles and thermal evolution to gamma-$Fe_2O_3$, J. Mater. Sci. 39 (2004) 4877–4885.
[19] W. Yi, W. MoberlyChan, V. Narayanamurti, Y.F. Hu, Q. Li, I. Kaya, M. Burns, D.M. Chen, Characterization of spinel iron-oxide nanocrystals grown on Fe whiskers, J. Appl. Phys. 95 (2004) 7136–7138.
[20] E.A. Shafranovsky, Y.I. Petrov, Aerosol Fe nanoparticles with the passivating oxide shell, J. Nanopart Res. 6 (2004) 71–90.
[21] V. Maurice, W.P. Yang, P. Marcus, XPS and STM investigation of the passive film formed on Cr (110) single-crystal surfaces, J. Electrochem. Soc. 141 (1994) 3016–3027.
[22] M.P. Ryan, R.C. Newman, G.E. Thompson, A scanning-tunneling-microscopy study of structure and structural relaxation in passive oxide-films on Fe-Cr alloys, Philos. Mag. B 70 (1994) 241–251.
[23] M.P. Ryan, R.C. Newman, G.E. Thompson, Atomically resolved STM of oxide film structures on Fe-Cr alloys during passivation in sulfuric-acid-solution, J. Electrochem. Soc. 141 (1994) L164–L165.
[24] V. Maurice, W.P. Yang, P. Marcus, XPS and STM study of passive films formed on Fe-22Cr (110) single-crystal surfaces, J. Electrochem. Soc. 143 (1996) 1182–1200.
[25] V. Maurice, W.P. Yang, P. Marcus, X-ray photoelectron spectroscopy and scanning tunneling microscopy study of passive films formed on (100) Fe-18Cr-13Ni single-crystal surfaces, J. Electrochem. Soc. 145 (1998) 909–920.
[26] T. Massoud, V. Maurice, L.H. Klein, P. Marcus, Nanoscale morphology and atomic structure of passive films on stainless steel, J. Electrochem. Soc. 160 (2013) C232–C238.
[27] L. Signorini, L. Pasquini, L. Savini, R. Carboni, F. Boscherini, E. Bonetti, A. Giglia, M. Pedio, N. Mahne, S. Nannarone, Size-dependent oxidation in iron/iron oxide core-shell nanoparticles, Phys. Rev. B 68 (2003) 195423.
[28] D.W. Kavich, J.H. Dickerson, S.V. Mahajan, S.A. Hasan, J.H. Park, Exchange bias of singly inverted FeO/$Fe_3O_4$ core-shell nanocrystals, Phys. Rev. B 78 (2008) 174414.
[29] J. Zhu, S. Wei, X. Chen, A.B. Karki, D. Rutman, D.P. Young, Z. Guo, Electrospun polyimide nanocomposite fibers reinforced with core-shell Fe-FeO nanoparticles, J. Phys. Chem. C 114 (2010) 8844–8850.
[30] A. Pratt, L. Lari, O. Hovorka, A. Shah, C. Woffinden, S.P. Tear, C. Binns, R. Kroeger, Enhanced oxidation of nanoparticles through strain-mediated ionic transport, Nat. Mater. 13 (2014) 26–30.
[31] D. Landolt, S. Mischler, A. Vogel, H.J. Mathieu, Chloride-ion effects on passive films on FeCr and FeCrMo studied by AES, XPS and SIMS, Corros. Sci. 31 (1990) 431–440.
[32] S. Mischler, A. Vogel, H.J. Mathieu, D. Landolt, The chemical-composition of the passive film on Fe-24Cr and Fe-24Cr-11Mo studied by AES, XPS and SIMS, Corros. Sci. 32 (1991) 925–944.
[33] R.H. Jung, H. Tsuchiya, S. Fujimoto, XPS characterization of passive films formed on type 304 stainless steel in humid atmosphere, Corros. Sci. 58 (2012) 62–68.
[34] P. Keller, H.H. Strehblow, XPS investigations of electrochemically formed passive

layers on Fe/Cr-alloys in 0.5 m $H_2SO_4$, Corros. Sci. 46 (2004) 1939–1952.
[35] N. Padhy, R. Paul, U.K. Mudali, B. Raj, Morphological and compositional analysis of passive film on austenitic stainless steel in nitric acid medium, Appl. Surf. Sci. 257 (2011) 5088–5097.
[36] H.H. Strehblow, Passivity of metals studied by surface analytical methods, a review, Electrochim. Acta 212 (2016) 630–648.
[37] S. Haupt, H.H. Strehblow, A combined surface analytical and electrochemical study of the formation of passive layers on Fe/Cr alloys in 0.5 m $H_2SO_4$, Corros. Sci. 37 (1995) 43–54.
[38] V. Vignal, H. Krawiec, O. Heintz, D. Mainy, Passive properties of lean duplex stainless steels after long-term ageing in air studied using EBSD, AES, XPS and local electrochemical impedance spectroscopy, Corros. Sci. 67 (2013) 109–117.
[39] S. Fajardo, D.M. Bastidas, M.P. Ryan, M. Criado, D.S. McPhail, R.J.H. Morris, J.M. Bastidas, Low energy SIMS characterization of passive oxide films formed on a low-nickel stainless steel in alkaline media, Appl. Surf. Sci. 288 (2014) 423–429.
[40] M. Salasi, G.B. Stachowiak, G.W. Stachowiak, M.R. Kilburn, NanoSIMS investigation of passive oxide films on high-Cr cast iron, Corros. Sci. 67 (2013) 298–303.
[41] A. Seyeux, V. Maurice, L.H. Klein, P. Marcus, In situ STM study of the effect of chloride on passive film on nickel in alkaline solution, J. Electrochem. Soc. 153 (2006) B453–B463.
[42] A.J. Davenport, M. Sansone, High-resolution in-situ XANES investigation of the nature of the passive film on iron in a pH 8.4 borate buffer, J. Electrochem. Soc. 142 (1995) 725–730.
[43] L.J. Oblonsky, A.J. Davenport, M.P. Ryan, H.S. Isaacs, R.C. Newman, In situ X-ray absorption near edge structure study of the potential dependence of the formation of the passive film on iron in borate buffer, J. Electrochem. Soc. 144 (1997) 2398–2404.
[44] P. Schmuki, S. Virtanen, H.S. Isaacs, M.P. Ryan, A.J. Davenport, H. Bohni, T. Stenberg, Electrochemical behavior of $Cr_2O_3/Fe_2O_3$ artificial passive films studied by in situ XANES, J. Electrochem. Soc. 145 (1998) 791–801.
[45] M. Murayama, N. Makiishi, Y. Yazawa, T. Yokota, K. Tsuzaki, Nano-scale chemical analyses of passivated surface layer on stainless steels, Corros. Sci. 48 (2006) 1307–1318.
[46] J.C. Rao, X.X. Zhang, B. Qin, K.K. Fung, TEM study of the structural dependence of the epitaxial passive oxide films on crystal facets in polyhedral nanoparticles of chromium, Ultramicroscopy 98 (2004) 231–238.
[47] E. Hamada, K. Yamada, M. Nagoshi, N. Makiishi, K. Sato, T. Ishii, K. Fukuda, S. Ishikawa, T. Ujiro, Direct imaging of native passive film on stainless steel by aberration corrected STEM, Corros. Sci. 52 (2010) 3851–3854.
[48] R. Soulas, M. Cheynet, E. Rauch, T. Neisius, L. Legras, C. Domain, Y. Brechet, TEM investigations of the oxide layers formed on a 316l alloy in simulated PWR environment, J. Mater. Sci. 48 (2013) 2861–2871.
[49] K. Oh, S. Ahn, K. Eom, K. Jung, H. Kwon, Observation of passive films on Fe-20Cr-xNi (x = 0, 10, 20 wt.%) alloys using TEM and Cs-corrected STEM-EELS, Corros. Sci. 79 (2014) 34–40.
[50] J.E. Castle, J.H. Qiu, The application of ICP-MS and XPS to studies of ion selectivity during passivation of stainless-steels, J. Electrochem. Soc. 137 (1990) 2031–2038.
[51] J.C. Rao, X.X. Zhang, B. Qin, K.K. Fung, High-resolution transmission electron microscopy study of epitaxial passive films on nanocubes of chromium, Philos. Mag. Lett. 83 (2003) 395–401.
[52] Kj Gallaghe, W. Feitknec, U. Mannweil, Mechanism of oxidation of magnetite to gamma-$Fe_2O_3$, Nature 217 (1968) 1118–1121.
[53] U. Colombo, G. Fagherazzi, F. Gazzarri, G. Lanzavecchia, G. Sironi, Mechanism of low temperature oxidation of magnetites, Nature 219 (1968) 1036-+.
[54] P.S. Sidhu, R.J. Gilkes, A.M. Posner, Mechanism of low-temperature oxidation of synthetic magnetites, J. Inorg. Nucl. Chem. 39 (1977) 1953–1958.
[55] T.W. Swaddle, P. Oltmann, Kinetics of the magnetite-maghemite-hematite transformation, with special reference to hydrothermal systems, Can. J. Chem. Revue Canadienne De Chimie 58 (1980) 1763–1772.
[56] A. Atkinson, Transport processes during the growth of oxide-films at elevated-temperature, Rev. Mod. Phys. 57 (1985) 437–470.
[57] J. Tang, M. Myers, K.A. Bosnick, L.E. Brus, Magnetite $Fe_3O_4$ nanocrystals: spectroscopic observation of aqueous oxidation kinetics, J. Phys. Chem. B 107 (2003) 7501–7506.
[58] A.R. Brooks, C.R. Clayton, K. Doss, Y.C. Lu, On the role of cr in the passivity of stainless-steel, J. Electrochem. Soc. 133 (1986) 2459–2464.
[59] S. Haupt, H.H. Strehblow, Corrosion, layer formation, and oxide reduction of passive iron in alkaline-solution - a combined electrochemical and surface analytical study, Langmuir 3 (1987) 873–885.